Frascati Physics Series Vol. nnn (2001), pp. 000-000
IX Int. Conf. on Calorimetry in Part. Phys. - Annecy, Oct. 9-14, 2000

PHYSICS PROCESSES IN HADRONIC SHOWERS

Alfredo Ferrari
CERN CH-1211, Geneva 23, Switzerland (on leave from INFN, Milan)
Paola R. Sala
CERN CH-1211, Geneva 23, Switzerland (on leave from INFN, Milan)

ABSTRACT

The paper describes a few basic features of nuclear interactions, relating them to quantities of interest for calorimetry. Some examples of comparison of experimental data for particle production with state-of-the-art model predictions are presented. A discussion of the impact of hadronic interactions on quantities of interest for calorimetry follows. Finally, some predictions of calorimetric performances are presented for the case of the ICARUS fully sensitive liquid argon detector as an example of a calorimeter limited only by the intrinsic fluctuations of hadronic showers, as well as for the ATLAS combined calorimeter test beam where experimental data are available.

1 Main steps of h-A interactions

The approach to hadronic interaction modelling presented here is the one adopted by most state-of-the-art codes. In this "microscopic" approach, each

step has sound physical basis. Performances are optimized comparing with particle production data at single interaction level. No tuning whatsoever on "integral" data, like calorimeter resolutions, thick target yields etc, is performed. Therefore, final predictions are obtained with minimal free parameters, fixed for all energies and target/projectile combinations. Results in complex cases as well as scaling laws and properties come out naturally from the underlying physical models and the basic conservation laws are fulfilled "a priori". All the examples/results presented in the following have been obtained with FLUKA [1, 2] and should be typical of codes adopting similar approaches.

High-energy h-A interactions can be schematically described as a sequence of the following steps:

- Glauber-Gribov cascade and high energy collisions
- (Generalized)-IntraNuclear cascade
- Preequilibrium emission
- Evaporation/Fragmentation/Fission and final deexcitations

A few aspects are of particular relevance for calorimetry, multiplicity distribution of fast (relativistic) particles, π^0 and γ production and its scaling with projectile energy, slow fragment and neutron production, the asymptotic regime of the target fragmentation part of the collision, and binding energy losses. These aspects, that are often interrelated, are developed in more details in the following. We refer to the literature for complete model descriptions and for exhaustive code validation [1, 2].

1.1 Hadron-nucleon interaction models

A comprehensive understanding of hadron-nucleon interactions over a large energy range is of course a basic ingredient for a sound description of hadron-nucleus ones. For what concerns elastic, charge exchange and strangeness exchange reactions, they are described by phase-shift analysis and/or fits of experimental differential data,and standard eikonal approximations are used at high energies. Two families of models are adopted for inelastic interactions, depending on the projectile energy: those based on resonance production and decays, which cover the energy range up to 3–5 GeV; those based on quark/parton string models, which provide reliable results up to several tens of TeV

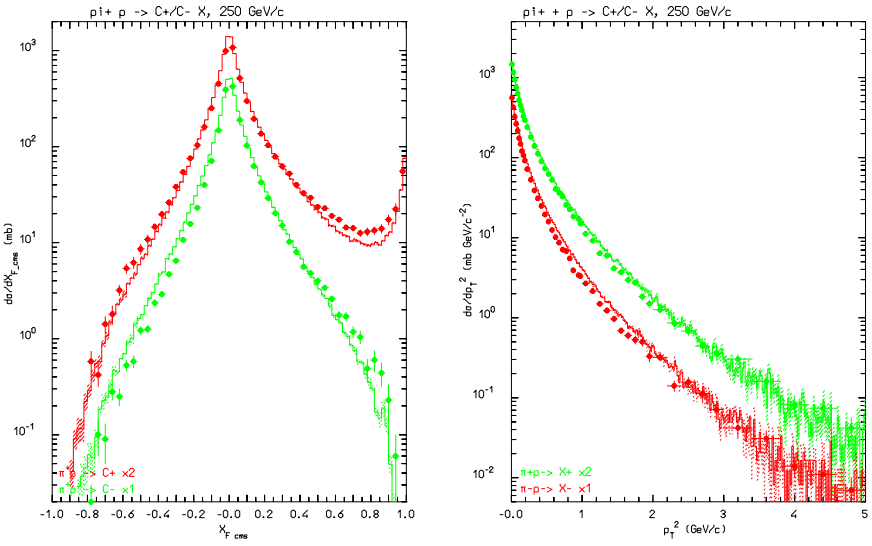

Figure 1: Feynman x_F^* (left) and p_t (right) spectra of positive and negative particles from (π^+,p) at 250 GeV/c . Exp. data (symbols) from [4].

1.1.1 h-N interactions at intermediate energies

The pion production channel in nucleon-nucleon interactions opens already around 290 MeV, and becomes important important above 700 MeV. In pion-nucleon interactions the production threshold is as low as 170 MeV. Both reactions are normally described in the framework of the isobar model: all reactions proceed through an intermediate state containing at least one resonance. For example:

$$\begin{aligned} N_1 + N_2 &\rightarrow N_1' + \Delta(1232) \rightarrow N_1' + N_2' + \pi \\ \pi + N &\rightarrow \Delta(1600) \rightarrow \pi' + \Delta(1232) \rightarrow \pi' + \pi'' + N' \\ N_1 + N_2 &\rightarrow \Delta_1(1232) + \Delta_2(1232) \rightarrow N_1' + \pi_1 + N_2' + \pi_2 \end{aligned}$$

Resonance energies, widths, cross sections, branching ratios are extracted from data and conservation laws, whenever possible. They can be inferred from inclusive cross sections when needed.

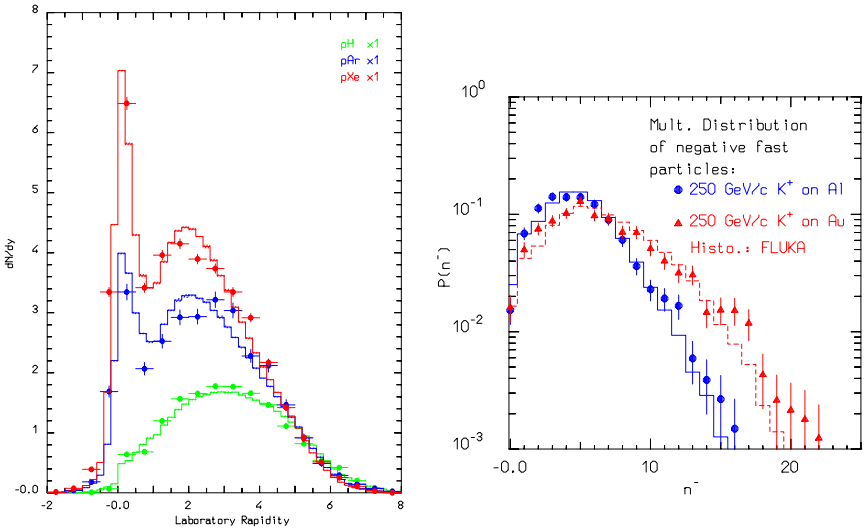

Figure 2: Rapidity distribution of charged particles produced in 200 GeV proton collisions on Hydrogen, Argon, and Xenon target (left), data from [7]. Multiplicity distribution of negative shower particles for 250 GeV/c K^+ on Aluminium and Gold targets (right), data from [8].

1.1.2 Inelastic hN interactions at high energies: (DPM, QGSM, ...)

The features of "soft" interactions (low-p_T interactions) cannot be derived from the QCD Lagrangian, because the large value taken by the running coupling constant prevents the use of perturbation theory. Models based on interacting strings emerged as a powerful tool in understanding QCD at the soft hadronic scale, that is in the non-perturbative regime. An interacting string theory naturally leads to a topological expansion. The Dual Parton Model [3] is one of these models and it is built introducing partonic ideas into a topological expansion which explicitly incorporates the constraints of duality and unitarity, typical of Regge's theory. In DPM hadrons are considered as open strings with quarks, antiquarks or diquarks sitting at the ends; mesons (colorless combination of a quark and an antiquark $q\bar{q}$): are strings with their valence quark and antiquark at the ends. At sufficiently high energies the leading term in the interactions corresponds to a Pomeron (IP) exchange (a closed string exchange), which has a cylinder topology. When an unitarity cut is applied to the cylindri-

cal Pomeron two hadronic chains are left as the sources of particle production. As a consequence of color exchange in the interaction, each colliding hadron splits into two colored system, one carrying color charge c and the other $\bar{c}$. The system with color charge c ($\bar{c}$) of one hadron combines with the system of complementary color of the other hadron, to form two color neutral chains. These chains appear as two back-to-back jets in their own centre-of-mass systems.

The chains produced in an interaction are then hadronized. DPM gives no prescriptions on this stage of the reaction. All the available chain hadronization models, however, rely on the same basic assumptions, the most important one being *chain universality*, that is chain hadronization does not depend on the particular process which originated the chain. As a consequence, fragmentation functions can in principle be derived from hard processes and e^+e^- data and the same functions and (few) parameters should be valid for all reactions and energies; actually mass and threshold effects are non-negligible at the typical chain energies involved in hadron-nucleus reactions. Transverse momentum is usually added according to uncertainty considerations. The examples in fig. 1 show the ability of the FLUKA, DPM based, model to reproduce the features of particle production; further examples can be found in [1, 2].

1.2 (Generalized) IntraNuclear Cascade basic assumptions

At energies high enough to consider coherent effects as corrections, a hadron-nucleus (hA) reaction can be described as a cascade of two-body interactions, concerning the projectile and the reaction products. This is the mechanism called IntraNuclearCascade (INC). INC models were developed already at the infancy of the computer era with great success in describing the basic features of nuclear interactions in the 0.2-2 GeV range. Modern INC models had to incorporate many more ideas and effects in order to describe in reasonable way reactions at higher and lower energies. Despite particle trajectories are described classically, many quantistic effects have to be incorporated in these (Generalized)INC models, like Pauli blocking, formation time, coherence length, nucleon antisymmetrization, hard core nucleon correlations. A thorough description of the (G)INC model used in FLUKA can be found in [1, 2].

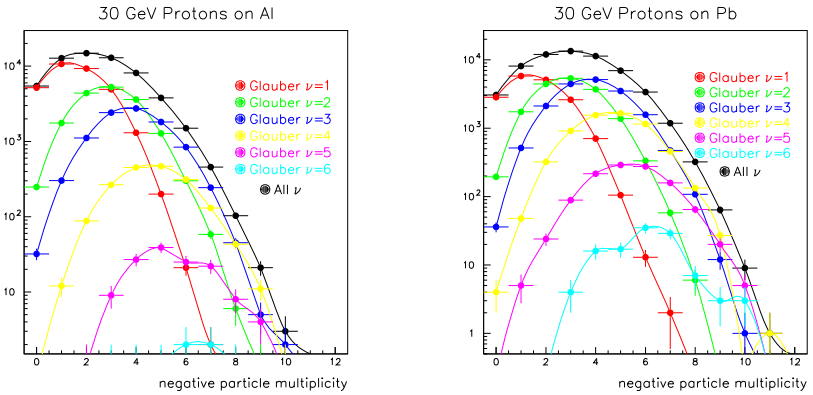

Figure 3: Negative particle multiplicity distribution for 30 GeV protons on Al (left) and Pb (right), total and for given numbers of primary collisions

1.3 h-A at high energies: the Glauber-Gribov Cascade

The Glauber [5] formalism provides a powerful and elegant method to derive elastic, quasi-elastic and absorption hA cross sections from the free hadron-Nucleon cross section and the nuclear ground state *only*. Inelastic interactions are equivalent to multiple interactions of the projectile with ν target nucleons. The number of such "primary" interactions follows a binomial distribution (at a given impact parameter, b):

$$P_{r\ \nu}(b) \quad \equiv \quad \left(\begin{array}{c} A \\ \nu \end{array} \right) P_r^{\nu}(b) \left[1 - P_r(b)\right]^{A-\nu}$$

where $P_r(b) \equiv \sigma_{hN\ r} T_r(b)$, and $T_r(b)$ is the profile function (folding of nuclear density and scattering profiles along the path). On average :

$$< \nu > \quad = \quad \frac{Z\sigma_{hp\ r} + N\sigma_{hn\ r}}{\sigma_{hA\ abs}}$$

$$\sigma_{hA\ abs}(s) \quad = \quad \int \mathrm{d}^2\vec{b} \left[1 - \left(1 - \sigma_{hN\ r}(s) T_r(b)\right)^A\right]$$

The Glauber-Gribov [6] model represents the diagram interpretation of the Glauber cascade. The ν interactions of the projectile originate 2ν chains, out of which 2 chains struck between the projectile and target valence (di)quarks,

$2(\nu-1)$ chains between projectile sea $q-\bar{q}$ and target valence (di)quarks. The distribution of the projectile energy among many chains naturally softens the energy distributions of reaction products (see fig. 2) and boosts the multiplicity with respect to hadron-hadron interactions (fig. 2). The building up of the multiplicity distribution from the multiple collisions is plotted in fig.3. In this way, the model accounts for the major A-dependent features without any degree of freedom, except in the treatment of mass effects at low energies.

The Fermi motion of the target nucleons must be included to obtain the correct kinematics, in particular the smearing of p_T distributions. All nuclear effects on the secondaries are accounted for by the subsequent (G)INC.

1.4 Formation Zone

The Formation Zone concept is essential to understand the observed reduction of the re-interaction probability with respect of the naive free cross section assumption. It can be understood as a "materialization" time. A qualitative estimate can be given as follows: in the frame where $p_{\|}=0$, the time necessary for materialization $\bar{t}$ is

$$\bar{t} \quad = \quad \Delta t \approx \frac{\hbar}{E_T} = \frac{\hbar}{\sqrt{p_T^2+M^2}}$$

Going to lab system

$$t_{lab} \quad = \quad \frac{E_{lab}}{E_T}\bar{t} = \frac{\hbar E_{lab}}{p_T^2+M^2}$$

The condition for possible re-interaction inside a nucleus is:

$$v \cdot t_{lab} \leq R_A \approx r_0 A^{\frac{1}{3}}$$

At high energies, the "fast" (from the emulsion language) particles produced in the Glauber cascade have a high probability to materialize already outside the nucleus without triggering a secondary cascade. Only a small fraction of the projectile energy is thus left available for the INC and the evaporation (see fig.6 and par. 1.8).

1.5 Preequilibrium

At energies lower than the π production threshold a variety of preequilibrium models have been developed [9] following two leading approaches: the quantum-mechanical multistep model and the exciton model. The former has very good

theoretical background but is quite complex, while the latter relies on statistical assumptions, and it is simple and fast. Exciton-based models are often used in MonteCarlo codes to join the INC stage of the reaction to the equilibrium one (see [2] for the FLUKA implementation).

1.6 Evaporation, fission and nuclear break-up

At the end of the reaction chain, the nucleus is a thermally equilibrated system, characterized by its excitation energy. This system can "evaporate" nucleons, or fragments, or γ rays, or even fission, to dissipate the residual excitation. The evaporation and fission probability for a particle of type j, mass m_j, spin $S_j \cdot \hbar$ and kinetic energy E are given by [10]

$$P_j = \frac{(2S_j+1)m_j}{\pi^2\hbar^3}\int_{V_j}^{U_i-Q_j-\Delta_f}\sigma_{\rm inv}\frac{\rho_f(U_f)}{\rho_i(U_i)}EdE$$

$$P_F = \frac{1}{2\pi\hbar}\frac{1}{\rho_i(U_i)}\int_0^{(U-B_F)}\rho_F(U-B_F-E)dE$$

Where ρ's are the nuclear level densities, U_i and U_f are the excitation energy of the initial and final nuclei, B_F is the fission barrier, Q_j the reaction Q for emitting a particle of type j, and $\sigma_{\rm inv}$ is the cross section for the inverse process, which takes into account a possible Coulomb barrier. Under standard approximations, the evaporation spectrum has a maxwellian shape:

$$P_j(E)dE \approx K\ E{\rm e}^{-\frac{E}{T}}dE$$

where T ($T \approx \sqrt{(U-\Delta)/a}$) is the nuclear temperature, usually in the MeV range (a: level density parameter $\approx A/8$ MeV^{-1}, Δ: pairing energy).

Neutron emission is favored over charged particle emission, due to the Coulomb barrier, expecially for medium-heavy nuclei. Moreover, the excitation energy is higher in heavier nuclei due to the larger cascading chances, and a is smaller, thus the average neutron energy is smaller. Therefore, the neutron multiplicity is higher for heavy nuclei than for light ones. For light residual nuclei, where the excitation energy may overwhelm the total binding energy, a statistical fragmentation (Fermi Break-up) model is more appropriate (see [1, 2, 11] for the FLUKA implementation).

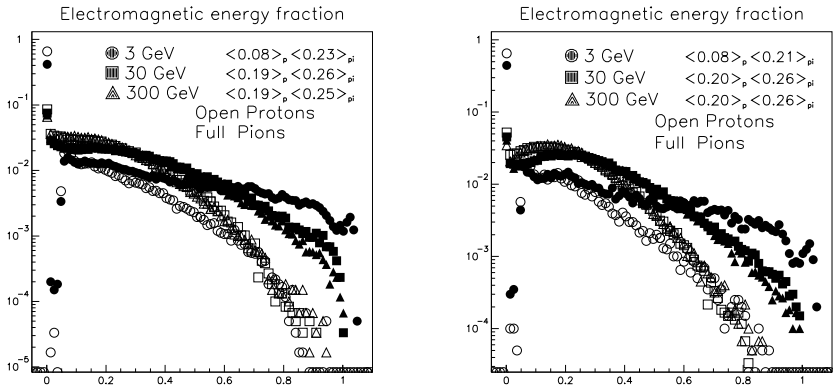

Figure 4: Distribution of the energy fraction carried by π^0's and γ's for interactions in aluminium (left) and lead (right)

1.7 h-A interactions: the electromagnetic component

Part of the projectile energy is converted into electromagnetic energy through the production of π^0 in the early stages of the reaction, and deexcitation γ at the end. At low energies, a few pions are produced in resonance reactions, and some reinteracts: the E.M. energy fraction is relatively small, with a broad distribution and a peak at zero (in low-energy π induced reactions, however, the charge exchange channel can result in fully electromagnetic events). The pion multiplicity grows with energy, and the formation zone quenches the reinteractions: the majority of energy goes into pions, and roughly a third of the pions are π^0. As seen in fig. 5, the asymptotic E.M. fraction is around 25% and 20% for pion and proton induced reactions, respectively. The π-proton difference is important for energy resolution, and comes essentially from the leading particle in the primary interaction. The distribution of the EM fraction is also different, the π one extending much further towards unity.

1.8 h-A at high energies: the invariance of the target fragmentation region

The Glauber cascade and the formation zone act together in reaching a regime where the "slow" part of the interaction is almost independent of the particle energy. This can be easily verified looking at charged particle average multiplicities and multiplicity distributions as a function of energy (fig.6). "Fast" tracks,

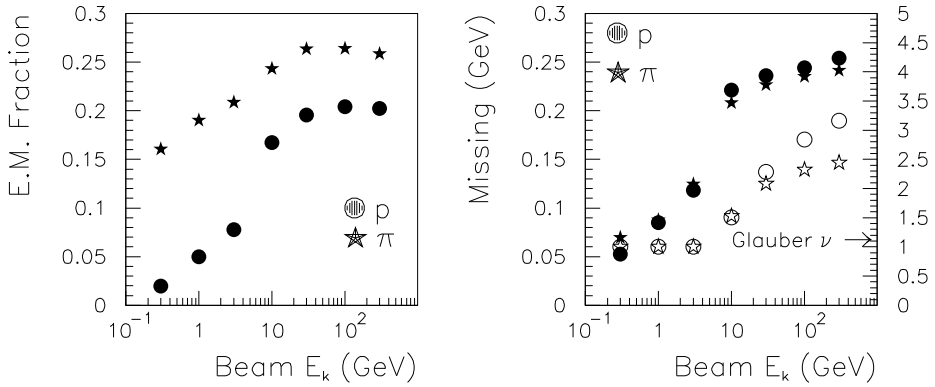

Figure 5: Average energy fraction carried by π^0's and γ's (left) and binding energy losses (right) for interactions in lead. The number of primary collisions are also reported in the last plot (open symbols)

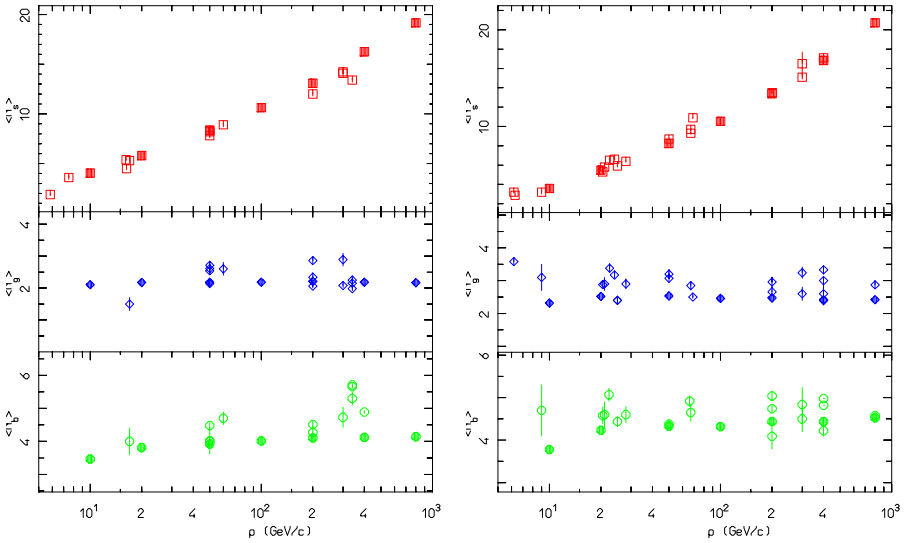

Figure 6: Shower, grey, and black tracks multiplicities for π^- (left) and protons (right) on emulsion, as a function of the projectile momentum. Open symbols are experimental data from various sources, full symbols are FLUKA results.

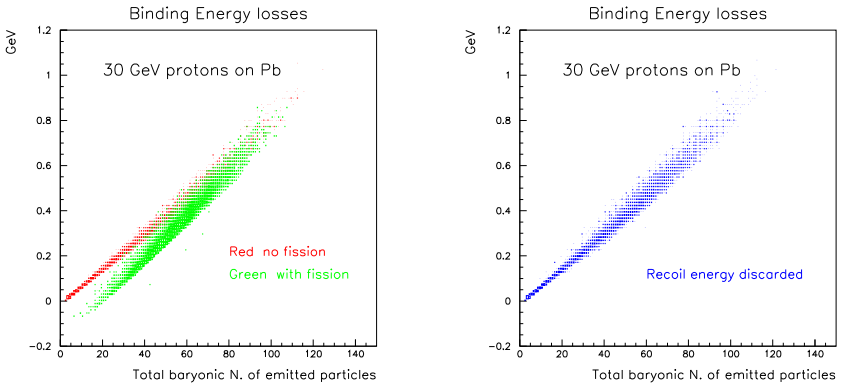

Figure 7: Binding energy losses for 30 GeV protons on lead (left). Binding energy losses plus heavy recoil energy for the same reaction (right)

coming from the projectile primary interactions, show the typical $\approx$ logarithmic increase observed for hN interactions. "Gray" tracks, mostly due to intranuclear cascade re-interactions tend to saturate just above 10 GeV. "Black" tracks, mostly due to evaporation charged particles saturate as well.

1.9 Energy conservation and its relevance for sound calorimetric calculations

A fraction of the incoming energy in hadronic interactions is spent via mass production. Binding energy losses and their fluctuations are an important ingredient, particularly at low projectile energies, both in determining the e/h ratio and the intrinsic resolution. A precise calculation of these losses can be easily performed using self-consistent interaction models fulfilling the basic conservations laws, energy, momentum and additive quantum numbers:

$$E_{k\ proj} + m_{proj} + {}^{A}_{Z}M \quad = \quad \sum_{i} [E_{k\ i} + m_i] + \sum_{j} \left[E_{k\ j} + {}^{A_j}_{Z_j} M_j\right]$$

Assuming that meson masses can be converted into signal (they either decay or are absorbed) and that antibaryons will eventually annihilate, giving twice of their mass to the signal, the net amount of visible energy, and the "lost" one (E_{loss}) with respect to the projectile will be: (I_{bar}=baryonic number)

$$E_{vis} \quad = \quad \sum_{i} [E_{k\ i} + (1 - I_{bar\ i}) \cdot m_i]$$

$$E_{loss} \quad = \quad \sum_i \left[I_{bar\ i} \cdot m_i \right] + \sum_j \left[{}^{A_j}_{Z_j} M_j \right] - I_{bar\ proj} \cdot m_{proj} - {}^{A}_{Z} M$$

Remembering the conservation of baryon number :

$$I_{bar\ diff} \stackrel{def}{=} A - \sum_j A_j = \sum_i I_{bar\ i} - I_{bar\ proj}$$

and assuming all baryon masses equal, and all binding energies equal to 8 MeV, it turns out that (obviously):

$$E_{loss} \quad \approx \quad 8 \times I_{bar\ diff} \text{ MeV}$$

This linear dependence and its spread is shown in fig.7 for a Pb target. In the case of heavy targets, like Pb, high energy fission releases energy, thus reducing the binding losses. However, in fig. 7 it is also shown the increase of E_{loss} when the kinetic energy of fission fragments and heavy recoils cannot be detected, as is the case in most real detectors. The behaviour of E_{loss} vs. beam energy is shown in fig.5. It saturates asymptotically at high energies, since the number of cascade and evaporation baryons stays constant, and the number of fast baryons follows approximately the number of Glauber collisions. Indeed, most baryons (many low energy neutrons) are produced during evaporation, while a few energetic baryons are emitted in the INC, and high energy primary collisions produce mainly mesons and baryon-antibaryon pairs.

1.10 The importance of in flight pion absorption

Both positive and negative pions can be absorbed in flight through multi-nucleon processes in nuclei. These processes are particularly important at subGeV energies (see [2]). For instance, competition with charge exchange strongly reduces the EM component, and weakly ionizing relativistic particles are converted into heavily ionizing protons and energetic neutrons, originating signal losses. This process impacts the e/h ratio at all energies as well as resolutions at low-medium energies. It is critical for Cerenkov calorimeters.

1.11 Quenching of heavily ionizing particle signals

An important contribution to calorimeter non compensation comes from quenching/recombination of signals (light, ionization...) in the sensitive medium. Highly ionizing tracks are the most affected, as shown in fig. 8.

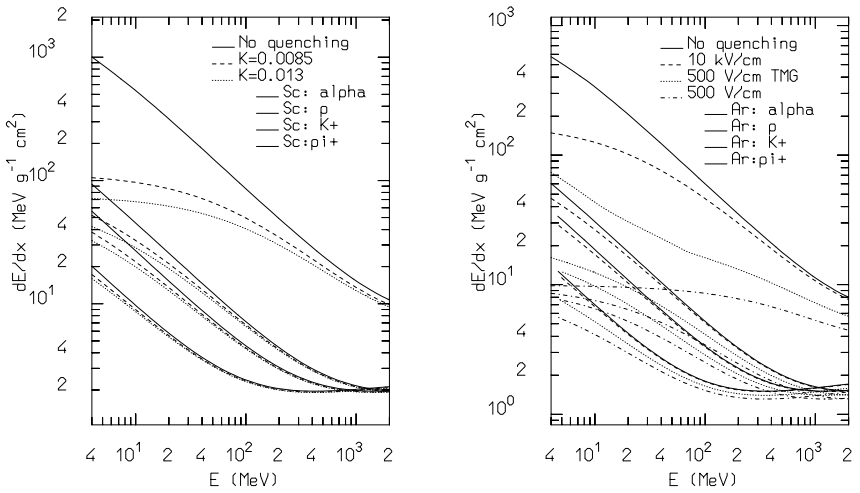

Figure 8: "Equivalent" stopping power for various particles in scintillator (left) and LAr (right) for some values of the quenching parameters

A phenomenological way to express the dependence of these effects on the ionization density is given by the Birks law:

$$\frac{dS}{d\rho x} = \left(\frac{dS}{dE}\right)_0 \frac{\frac{dE}{d\rho x}}{1 + K\frac{dE}{d\rho x} + ...}$$

Some typical values are :

- K for organic scintillators: $\approx$0.0085–0.013 (MeV/gr/cm^2)$^{-1}$
- K for LAr around 10 kV/cm: $\approx$0.005–0.007 (MeV/gr/cm^2)$^{-1}$
- K for LAr around 400–500 V/cm: $\approx$0.11 (MeV/gr/cm^2)$^{-1}$
- K for LAr around 400–500 V/cm with TMG doping [12]: $\approx$0.05 (MeV/gr/cm^2)$^{-1}$

1.12 "Low" energy neutrons

The fraction of energy carried by neutrons below 10-20 MeV (mostly evaporation neutrons) is very significant. Most of their kinetic energy is spent via elastic interactions, whose recoils are usually heavily quenched or even non ionizing, except in the case of scattering on hydrogen.

The low energy neutron contribution to the visible signal comes largely from γ rays, mostly from capture (from now on, γ_{sn}). In principle, if the γ_{sn} contribution could be fully accounted for most of the binding energy losses would be recovered. The capture probability is maximal in the thermal region. Thermalization times can vary from μs to ms depending on the material.

2 Infinite homogeneous calorimeters: some examples

Shower calculations at energies ranging from 1 to 300 GeV have been performed using infinite and homogeneous targets (Al, Fe, Pb and U), in order to score the various contributions to a possible signal, together with the energy lost for binding and neutrinos.

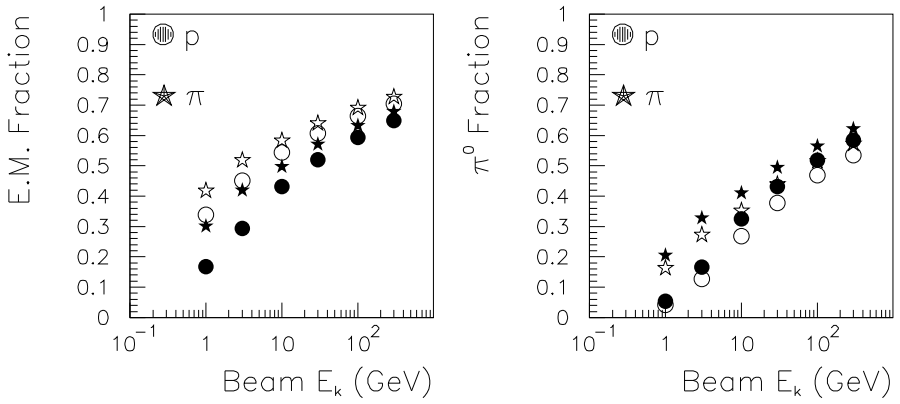

Figure 9: Energy fraction carried by π^0's and γ's for π and proton showers (left). The same without the γ_{sn} contribution (right). Open symbols: Pb, Full symbols: Fe

2.1 The electromagnetic component

Due to the possibly different response to electromagnetic (EM) and hadronic energy deposit and to binding energy losses which are inherently linked with the hadronic part of a cascade, the ratio of energy spent into γ's and π^0's is a critical parameter for calorimetry. Fig. 9 shows the behaviour of the fraction of EM energy as a function of the beam energy for proton and pion projectiles on Lead and Iron targets. The plot with the contribution of γ_{sn} removed is the

most significant (see the next paragraphs for a discussion of the role of γ_{sn}'s). The EM fraction is increasing with the beam energy, and will eventually become one at very high energies, as expected, since the fraction going into π^0's tends to be constant in each interaction. There is a significant difference between pion and proton beams at low-medium energies, with the former producing showers richer in EM energy (i.e. 0.34 against 0.27 at 10 GeV on lead), which is washing out as expected at the largest energies. However one should not forget that the EM fraction of the first interaction remains different also at higher energies (see paragraph 1.7) with possible impacts on the resolution.

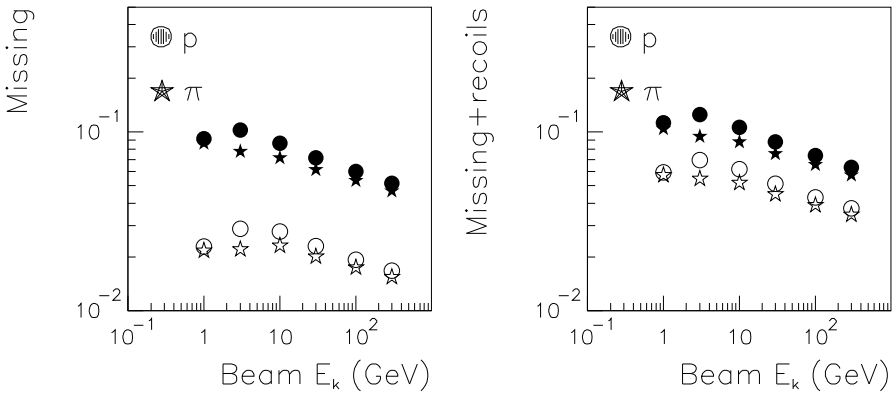

Figure 10: Average energy fraction "lost" due to binding for pion and proton showers (left). The same with in addition the energy due to heavy recoils and fission fragments (right). Open symbols: Pb, Full symbols: Fe.

2.2 Binding losses

The evolution of fractional binding energy losses as a function of pion and proton energy for Lead and Iron is shown in fig. 10. The right part of the figure includes in the missing balance also the kinetic energy of "heavy" (heavier than α's) recoils and fission fragments, which usually cannot be detected because they are not ionizing (elastic recoils), or confined outside the active medium (fission fragments). The energy carried by γ_{sn} is assumed to be detectable and it is not counted as lost (see the next paragraphs). The apparent large difference in the left plot between Pb and Fe is mostly due to fission fragments (high

energy fission is possible on Lead). There is still a slight difference once "heavy" recoils are counted as lost. The reason is that Lead is likely to produce a larger neutron to proton ratio in the evaporation stage of the interactions: while the binding energy spent for producing a neutron can be eventually recovered through capture γ's, that for a proton is definitively lost when it is ranged out.

As expected on the basis of the considerations outlined in section 1, the fractional binding energy loss is decreasing with increasing energy, since the absolute energy lost per interaction is approximately constant at high energy and furthermore more and more energy flows in the EM sector without giving rise to nuclear interactions.

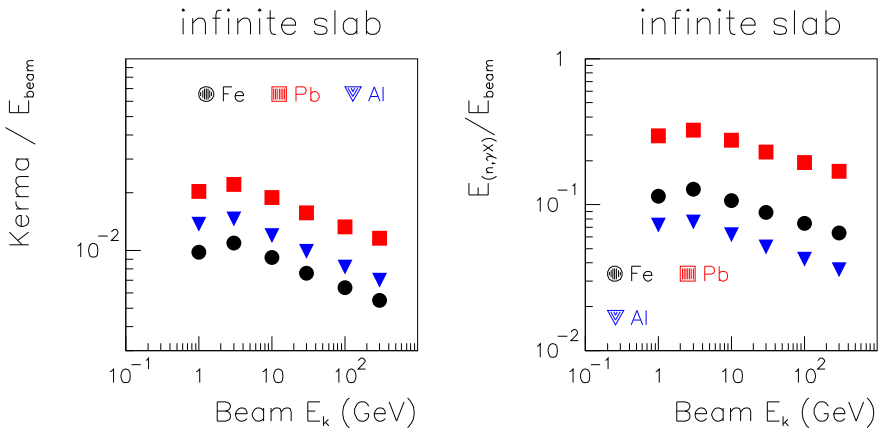

Figure 11: Average fractions of energy carried by "slow" neutrons, kinetic (left), and by γ's produced in (n,n') and capture reactions (right)

2.3 The role of slow neutrons

Low energy neutrons (customarily defined as neutrons with energies lower than 20 MeV) are (see section 1) the most important tracers of binding energy losses, hence their detection has a key role in calorimetry. Neutrons carry energy in two ways: kinetic energy (kerma), which is mostly transferred to charged particle recoils through elastic scattering, and a "potential" energy associated with their capture. If they do not escape the system, they will eventually be

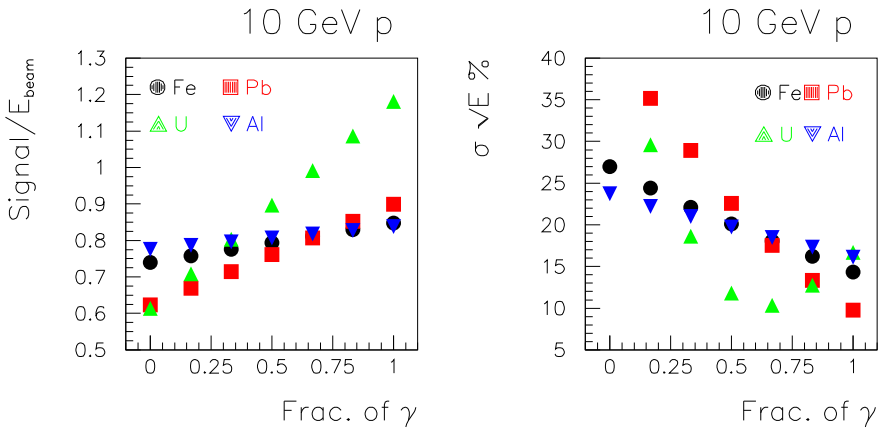

Figure 12: Average "visible" signal (left) (heavy recoil excluded, no quenching) and fractional resolution (right) as a function of the collected fraction of γ_{sn}

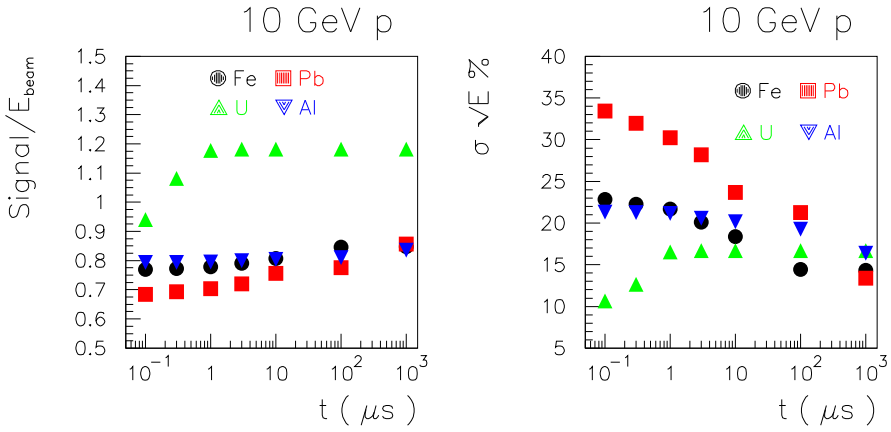

Figure 13: Average "visible" signal (left) (heavy recoil excluded, no quenching) and fractional resolution (right) as a function of integration time. The time scales are meaningful only for the given materials, hydrogen content could significantly affect neutron thermalization times

captured releasing the resulting binding energy in the form of photons.

The fraction of (beam) energy carried by slow neutrons in both forms is plotted in fig. 11 for proton projectiles on Al, Fe and Pb. It is important to

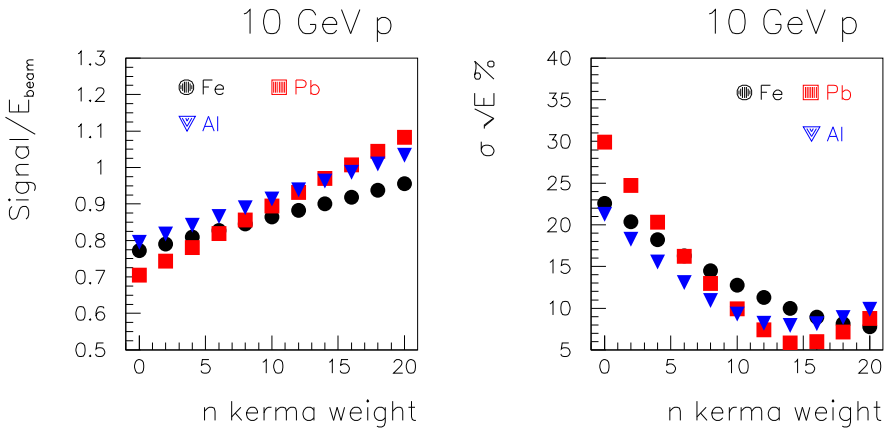

Figure 14: Average "visible" signal (left) (heavy recoil excluded, 30% of γ_{sn}, no quenching) and fractional resolution (right) as a function of the enhancement of the slow neutron kinetic energy signal (i.e. using hydrogen in the sensitive medium)

remark that the energy carried by γ_{sn} is of the order of 30 % around 10 GeV in lead: if these photons cannot be detected (i.e. because they come too late), the overall amount of "missing" visible energy will approach 40 % (summing with the left plot of fig. 10). According to the previous discussion, there are two possible ways of sampling properly the contribution of slow neutrons, either detecting efficiently their elastic recoils, or collecting the signal from the associated photons (or both). In both cases the active medium should oversample these contributions with respect to the passive material in order to achieve compensation. If not, the unavoidable energy losses (binding due to ranged out protons, neutrinos, quenching of slow charged particles) cannot be fully recovered. Oversampling of photons is pretty hard, since it is rather the opposite if the active medium has a lower Z than the passive one and, more important, their time delays can prevent the detection of a significant fraction in most practical situations. On the other hand, oversampling of the kinetic energy contribution can be easily accomplished using a hydrogenated active medium. The oversampling factor must be quite large in order to compensate for the possible missed detection of capture photons (and anyway capture in hydrogen produces only a 2.2 MeV photon with a severe loss wrt the energy

spent in producing the neutron). The case of fissionable materials (uranium) is special since both energy contributions are strongly boosted by the neutron multiplication process; it will be discussed in the following.

To better illustrate the influence of these mechanisms, the average fraction of visible energy (no heavy recoil, no quenching) and the fractional energy resolution (in units of $\% \times \sqrt{E}$ [1]) will be presented in the following for some representative situations, for a 10 GeV proton beam on various materials. The conclusions are general and do not depend on the projectile/energy combination chosen for the examples.

In figs. 12 and 13, these quantities are presented as a function of the fraction of γ_{sn} detected and of the acceptance time window respectively, for Al, Fe, Pb and U targets. Obviously the best resolutions correspond to the cases where the "visible" signal is close to one, that is full compensation is achieved. It is important to stress that for Al, Fe and Pb this condition is never fulfilled (no way for an infinite homogeneous target to oversample those photons): furthermore the time required to collect most of the γ signal is unacceptably large for most practical situations. The burden of missing a significant fraction of these photons is particularly heavy for lead, as expected, where the production of evaporation neutrons is at maximum. Uranium shows a completely different pattern: neutron multiplication through fission produces a strong excess signal and the time delay of photons is very short. Clearly compensation can be achieved sampling only a fraction of these photons in a relatively short time window without the need for hydrogenated readout. It is also worthwhile to note that despite the presented examples are for infinite homogeneous "calorimeters" and hence they do not include any sampling fluctuation, the fractional resolution can be rather poor (worse than $40\%/\sqrt{E}$ for lead) if only a small fraction of the energy carried by these photons is detected.

Fig. 14 shows again the average "visible" signal (no heavy recoils, no quenching and 30% of slow neutron photons detected) and the fractional energy resolution, this time as a function of a (possible) slow neutron kinetic energy release (kerma) oversampling factor. Such a factor can only be achieved in sampling calorimeters with hydrogenated readout. In this case, under the simple assumption that all the slow neutron kinetic energy will be released to

[1] This is only to give numbers in familiar units, in reality σ includes also a constant term

hydrogen, the plotted kerma weighting factor is nothing else that the inverse of the calorimeter sampling fraction. Inspection of the figures shows that compensation can be achieved for lead with a sampling fraction of the order of 6% and the resulting intrinsic resolution could be as small as 5-6%/$\sqrt{E}$. These numbers must be taken as qualitative since they depend on many assumptions, and could come out different if signal quenching is present or the fraction of γsn detected is different from the value, 30%, assumed for the example.

3 Examples

Medium	Compensation	Quench corr.	Resolution
Pure argon	no	no	$27\%/\sqrt{E} \oplus 8\%$
	yes	no	$24\%/\sqrt{E} \oplus 4\%$
	no	yes	$18\%/\sqrt{E} \oplus 6\%$
	yes	yes	$16\%/\sqrt{E} \oplus 1\%$
TMG doped argon	no	no	$20\%/\sqrt{E} \oplus 6\%$
	yes	no	$16\%/\sqrt{E} \oplus 2\%$
	no	yes	$15\%/\sqrt{E} \oplus 5\%$
	yes	yes	$12\%/\sqrt{E} \oplus 0.2\%$
No quenching	no	–	$15\%/\sqrt{E} \oplus 5\%$
	yes	–	$12\%/\sqrt{E} \oplus 0.1\%$

Table 1: Expected resolution in the liquid target for pions with and without TMG doping, showing the effect of the offline compensation and quench correction. For reference, the resolution that would be obtained with no recombination effects is also listed.

3.1 ICARUS: a test of the intrinsic limit of hadron calorimetry

The LAr TPC technique is based on the fact that ionization electrons can drift over large distances in a volume of purified liquid Argon under a strong electric field. With a proper readout system it is possible to realize a superb 3D imaging. The ICARUS collaboration has developed this technique and it is now ready to test the first large scale detector (the so called T600 detector, 600 tons of LAr). A larger detector, ICANOE has been recently proposed [13)]

for neutrino and rare event detection at Gran Sasso. Liquid argon is a non-compensating medium. When used in a time projection chamber like ICARUS the effect is exacerbated by the relatively low electric field ($\approx$ 300–500 V/cm) (see paragraph 1.11). However, the medium appears as a completely homogeneous volume with very high readout granularity, hence from the event visualization and from the local charge deposition density, it is possible both to distinguish between electromagnetic and hadronic components of a shower and to approximately correct for the recombination effects. Both corrections can be introduced at the analysis level.

Let assume that each elementary cell contains only one crossing track, the recombination effect can be unfolded using the collected charge and cell width to construct the observed dQ/dx and solving the recombination expression for the "actual" dE/dx. Despite its simplicity, the procedure is very promising in recovering most of the recombination, particularly when the Argon is doped with TMG [12].

When reconstructing the energy, assuming that electromagnetic energy deposition can be distinguished from hadronic one, the total energy of a shower is obtained as the sum of two terms $E = w \times (Q_{em} + \alpha \times Q_{had})$, where α is the compensation factor. In reality the discrimination between hadronic and electromagnetic energy depositions will have some inefficiency, mostly close to interaction points and when significant overlap occurs. For pure argon, for electric fields of $\approx$ 500 V/cm, α turns out to be about 1.5 (2.8) with and without quenching corrections respectively. The same figures for TMG-doped argon are 1.5 and 2.0.

The expected hadronic resolution for pions in the ICANOE detector is detailed in table 1.

3.2 ATLAS combined calorimeter test beam

The ATLAS Electromagnetic (Pb-LiquidArgon accordion geometry) and Hadronic (Fe-scintillator tiles) calorimeter prototypes have been tested together in 1994 and 1996 with π, μ and electron beams, from 10 to 300 GeV/c. Details of the layout and of the data analysis can be found in [15]. The same set-up has been simulated with FLUKA. Simulations have been compared with π and μ [14] data, trying to apply the same cuts as in the experimental analysis. Charge collection and signal quenching were simulated, while electronic noise

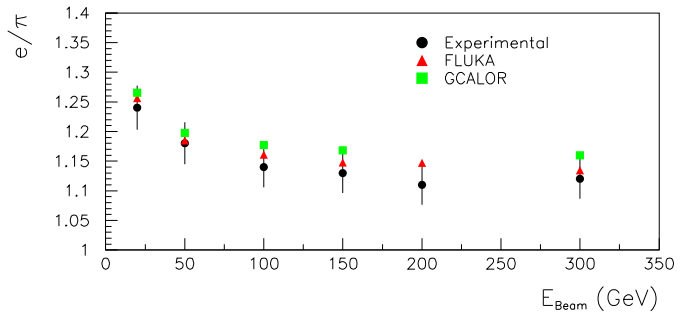

Figure 15: e/π signal ratio as a function of energy in the 1994 ATLAS combined calo test beam

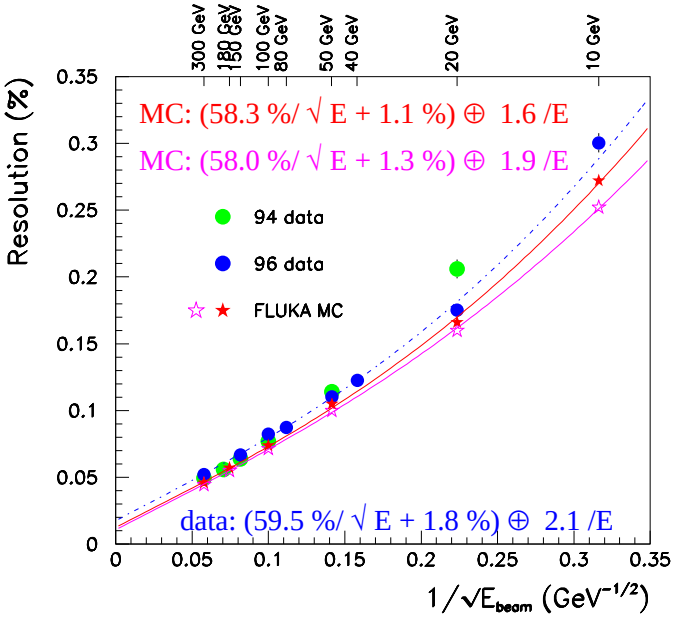

Figure 16: Fractional energy resolution in the ATLAS combined calo test beams

and photo-statistics were added a posteriori. Proton contamination in the pion beam has also been included.

The FLUKA results have been calibrated *in electron scale* without any

	a (GeV/pa)	b	c (GeV^{-1})
FLUKA	0.172(2)	0.38(2)	-0.00038(10)
EXP	0.172	0.44	-0.00038

Table 2: FLUKA and experimental (1994 data) parameters of the "benchmark" energy reconstruction

further normalization. The visible energy has been reconstructed using the "benchmark" technique: (see [15])

$$E_0 = E_{em} + a \cdot Q_{had} + b \cdot \sqrt{|E_{em_3} \cdot a \cdot Q_{had_1}|} + c \cdot E_{em}^2 \qquad (1)$$

All parameters have been fixed to minimize $\frac{\sigma}{E_0}$ at 300 GeV. FLUKA and experimental parameters are very similar, as shown in tab. 2; this certifies the correct simulation of sampling fractions and shower development, and adds significance to the other comparisons. The non-compensation as a function of energy (fig. 15) is also well described. The fractional energy resolution for the two test periods is shown in fig.16. The sampling term is well reproduced by FLUKA, the constant and noise terms are slightly underestimated. In the data, the lowest energy data points are affected by beam impurities, due to particles interacting in dead materials upstream the calorimeter. This contamination was dramatic in the 1994 20 GeV point, and has been fairly reduced in 1996 due to a better presampler module, that acted as a veto after a fairly complex cluster reconstruction. Nevertheless, the beam "dirtiness" was not completely under control. The two FLUKA sets in fig. 16 refer to two algorithms of cluster reconstruction in the presampler, both supposed to be corresponding to the experimental one, and show the sensitivity of the low energy results to the performance of this device.

E(GeV)	Per Interaction		Per Shower		σ/E	
	E_{miss}	rms	E_{miss}	rms	FLUKA	FLUKA+E_{miss}
10	0.094	0.25	2.1	0.93	24%	35%
100	0.070	0.28	12.7	5.3	7.2%	11.4%

Table 3: 10 GeV π^+ in the ATLAS 1996 Combined Calo set-up, with and without energy unbalance (E_{miss}) added at each interaction (see text).

3.2.1 The effect of energy non-conservations

A toy model has been set-up to give a quantitative feeling of the effects of energy non conservation in reaction modelling. A variable energy non-conservation has been applied, a posteriori, to the secondaries of each FLUKA simulated interaction. The central and rms values of this unbalance were chosen equal to those observed in the old GEANT3-GHEISHA package as a function of projectile/energy [16]. The procedure has been applied to π simulations in the ATLAS combined calo set-up. The first two columns of tab. 3 report the central and rms missing averaged over all the interactions in a shower; these energy errors build up in the development of the shower, leading to 10%-20% deviations in the global energy balance (the "per shower" columns of tab. 3). The effect on the fractional energy resolution (tab. 3) is dramatic, with increases of the order of 50%. Therefore the enforcement of energy and momentum conservation at each step is as important as having sound physical models.

4 Conclusions

Hadron interaction modelling is enough advanced to provide reliable estimates of particle production and propagation under most circumstances. Most of the basic features of hadronic calorimetry can be understood in terms of specific aspects of hadron nuclear interactions. All aspects related to energy conservation and binding energy losses are critical and deserve a proper treatment. Slow neutrons are "by construction" a precise index of the amount of energy going into binding. A proper sampling of their signal, via nuclear γ's detection or oversampling of their recoils (hydrogen) is critical in order to reduce the intrinsic resolution. The intrinsic resolution of hadronic showers is an ill-defined concept. Together with e/h it can vary wildly depending on the acceptance time window and quenching properties, for the same bulk characteristics. Reasonable predictions for real life calorimeters can be obtained provided reliable models are used and with a deep understanding of all instrumental effects.

Acknowledgements

The authors acknowledge the stimulating discussions and suggestions from G. Battistoni and C. Fabjan.

References

1. A. Fassò *et al* in Proc. SARE-3, KEK-Tsukuba, (ed H. Hirayama, May 7–9 1997) KEK report Proceedings 97-5, (1997) 32; A. Fassò *et al*, "Electron-photon transport in FLUKA: status", and "FLUKA: Status and Perspectives for Hadronic Applications", in MC2000 (Lisbon, Oct. 2000) (in press).
2. A. Ferrari, and P.R. Sala, in: Proc. Workshop on Nuclear Reaction Data and Nuclear Reactors Physics, Design and Safety, (ed. A. Gandini, G. Reffo, Trieste, Italy, April 1996), **2**, 424 (1998).
3. A. Capella *et al*, Phys. Rep. **236**, 225 (1994).
4. M. Adamus, Z. Phys. **C39**, 311 (1988).
5. R.J. Glauber and G. Matthiae, Nucl. Phys. **B21**, 135 (1970).
6. V.N. Gribov, Sov. Phys. JETP **29**, 483 (1969); V.N. Gribov, Sov. Phys. JETP **30**, 709 (1970); L. Bertocchi, Nuovo Cimento **11A**, 45 (1972).
7. C. De Marzo *et al*, Phys. Rev. **D26**, 1019 (1982)
8. I.V. Ajinenko *et al*, Z. Phys. **C42**, 377 (1989).
9. E. Gadioli, and P.E. Hodgson, Pre-equilibrium Nuclear Reactions, (Clarendon Press, Oxford, 1992).
10. V.F. Weisskopf, Phys. Rev. **52**, 295 (1937).
11. A. Ferrari *et al* Z. Phys. **C70**, 413 (1996).
12. P. Benetti *et al*, Nucl. Instr. and Meth. **A355** 660 (1995).
13. The ICANOE coll., CERN/SPSC 99-25, SPSC/P314 (1999).
14. M. Antonelli *et al* in: Proc. VI Int. Conf. on Calorimetry in High Energy Physics, (ed. A. Antonelli et al ,Frascati, June 1996), 561 (Frascati Physics Series, 1997).
15. Z. Ajaltouni *et al*, Nucl. Instr. Meth. **A387**, 333 (1997); S. Akhmadaliev *et al*, Nucl. Instr. Meth. **A441**, 461 (2000).
16. A. Ferrari and P.R. Sala, ATLAS Internal Note PHYS-NO-086 (1996)